

Supporting Information (SI)

Electrostatic promotion of the catalyst activity for ammonia
photosynthesis upon a robust affordable nanostructured uni-electrode
photodevice/reactor

Mohsen Lashgari^{a,b*} and *Parisa Zeinalkhani*^a

^a Department of Chemistry, Institute for Advanced Studies in Basic Sciences (IASBS),

Zanjan 45137-66731, Iran

^b Center for Research in Climate Change and Global Warming: Hydrogen and Solar Division,

Zanjan 45137-66731, Iran

* Corresponding author. Tel.: +98 24 33153205; fax: +98 24 33153232. *E-mail address:*

Lashgari@iasbs.ac.ir

This supporting document includes the following sections, figures and table:

- 1- Photodevice fabrication: cathodic electrodeposition of FeS₂ thin-film on Cu substrate
- 2- Film characterization: XRD, Raman, SEM, optical and electrical measurements
- 3- Electrochemical/photoelectrochemical tests
- 4- N₂-photofixation, ammonia analysis, and control experiments
- 5- Electrostatic promotion of the ammonia photosynthesis: applying a non-faradic potential bias to the photodevice

Fig. S1: LSV (a; scan rate 1 mV/s) and chronoamperometric (b; E= -0.9 V vs. Ag/AgCl, 3M) diagrams of the cathodic electrodeposition of FeS₂ on copper substrate (the inset is digital photograph of the fabricated FeS₂/Cu photodevice).

Fig. S2: XRD patterns of: (a) FeS₂ thin-film electrodeposited on the copper substrate, (b) Cu without thin film [recorded for the substrate before the electrodeposition process].

Fig. S3: SEM images (Top-view) of FeS₂ thin-film electrodeposited on the copper substrate, taken at different magnifications.

Fig. S4: Cross-sectional SEM image (Bird's-eye view) of the porous FeS₂ thin-film electrodeposited on the Cu substrate.

Fig. S5: Tauc's plot of the electrodeposited FeS₂ thin-film.

Fig. S6: UV-vis (a) and calibration (b) diagrams recorded in this study for determination of ammonia concentration through Nessler's approach (in the calibration diagram, absorbance was read at 425 nm).

Fig. S7: ¹H NMR spectra of ammonium (¹⁴NH₄⁺) aqueous media measured at different known concentrations (a) in the presence of p-benzoquinone [3.85 μM, serving as a reference for integral area determination]. (b) Calibration diagram for the ammonium solutions depicted using ¹H NMR data.

Fig. S8: ¹H NMR spectra of ammonium-15N sulfate (Sigma-Aldrich; (¹⁵NH₄)₂SO₄; 98 atom%) aqueous solutions measured at different known ammonium concentrations (a) in the presence of p-benzoquinone (3.85 μM). (b) Calibration diagram plotted for ¹⁵NH₄⁺ solutions using ¹H NMR data.

Fig. S9: Control experiments carried out for the synthesis of ammonia upon FeS₂/Cu monolithic photodevice.

Fig. S10: Stability/durability test of the photodevice for prolonged application to produce ammonia, recorded for four 24-h successive operations of the reactor.

Fig. S11: Promotion effect of alkali metal cations on the photodevice activity to produce ammonia [0.2 mM is the optimum concentration for the system under study; see **Fig. 7** of the main article].

Fig. S12: Schematic representation of applying a non-faradic/electrostatic dc potential bias to the photodevice (for accurate measurement of OCP data, the Potentio-Galvanostat instrument is employed).

Fig. S13: Ammonia photosynthesis under negative (a) and positive (b) non-faradic potential biases, recorded in a wide potential range, 0 to -300 V_{Earth}.

Fig. S14: Extra control experiments carried out for the ammonia synthesis under biased (B) and un-biased (U) conditions in the presence (I) and absence (D) of light [data were collected after 2 h operation of the photoreactor].

Fig. S15: Ionic chromatograms recorded for various sulfite/sulfate-containing media: (a) the reaction medium after 24 h operation of the photoreactor, (b) a synthetic/simulated reaction medium (sulfite (1160 μM) + sulfate (40 μM)), (c) sulfite solution (1.2 mM), and (d) sulfate solution (1.2 mM).

Table S1. A comparison of the ability of photoelectrochemical devices/reactors to synthesis ammonia between this work [utilizing low-price/earth-abundant/eco-friendly energy materials] and other related works reported in the literature.

1- Photodevice fabrication: cathodic electrodeposition of FeS₂ thin-film on Cu substrate

To fabricate the FeS₂/Cu photodevice, we utilized a commercially available pure copper sheet (thickness: 3mm, purity: 99.99% [1]), cut in the dimensions of 1.4×1cm². Prior to carrying out the electrodeposition process, the copper plate was chemically cleaned in a concentrated HCl solution [2] and washed thereafter using distilled water. The electrodeposition process was conducted in a conventional three-electrode cell, including Pt foil (2.5 cm²), Cu specimen (plate), and Ag/AgCl (3M), as a counter (CE), working (WE), and reference (RE) electrodes, respectively. The electrolyte was an aqueous solution containing 0.01 M ferrous cation (prepared from ammonium ferrous sulfate: (NH₄)₂Fe(SO₄)₂·6H₂O, 99%; Fluka) and 0.02 M sulfur source (sodium thiosulfate: Na₂S₂O₃·6H₂O, 99.5%; Merck); the pH of medium was set 3.8 using a dilute sulfuric acid (0.01 M) solution. The electrodeposition of FeS₂ thin-film was performed at 298 K using an IVIUM-VERTEX POTENTIOSTAT/GALVANOSTAT in a potentiostatic mode, by applying -0.9 V to WE (w.r.t. RE) for 400 sec [3]; the value -0.9 V is the potential being recognized for starting the film deposition (**Fig. S1a**). At the end of process, WE was removed from the electrodeposition bath, rinsed with deionized water, and finally annealed in Ar atmosphere for 25 min at 473 K [3].

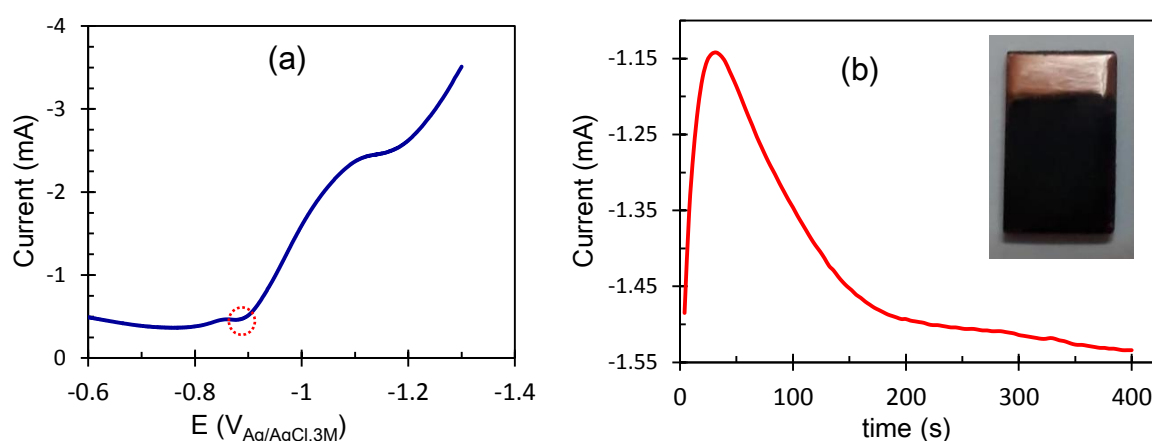
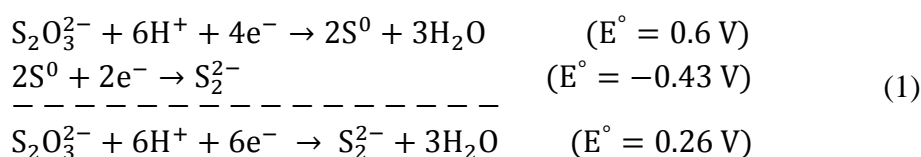


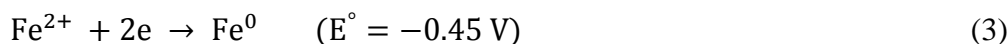
Figure S1. LSV (a; scan rate 1 mV/s) and chronoamperometric (b; E= -0.9 V vs. Ag/AgCl , 3M) diagrams of the cathodic electrodeposition of FeS₂ on copper substrate (the inset is digital photograph of the fabricated FeS₂/Cu photodevice).

Concerning the mechanism of FeS₂ electrodeposition, it should be mentioned that under a cathodic regime in acidic media, thiosulfate anion is reduced to disulfide (**eq. 1**) [4-5]. By the formation of disulfide at the metal/solution interface, Fe²⁺ is deposited and appears as a black insoluble FeS₂ film upon the WE (Cu) surface (**eq. 2**):





For the electrochemical deposition of FeS₂, the other suggested alternative route, is based on ferrous reduction (**eq. 3**) on the cathode surface [4]:



Here, the resulting Fe atoms could subsequently react with sulfur atoms and appear as a black FeS₂ film upon the copper substrate.

2- Film characterization: XRD, Raman, SEM, optical and electrical measurements

To affirm the formation of iron disulfide on the electrode surface, X-ray diffraction (XRD) analysis was conducted on the photodevice (FeS₂/Cu) using a PANalytical (Philips) X'pert PRO MRD (XL) instrument. Since the XRD peaks of the copper substrate were strong and the peak intensity of FeS₂ thin-film was extremely weak in comparison to that of substrate, the XRD pattern of FeS₂ appeared in the baseline, as some low-intensity background peaks (**Fig. S2**). Therefore, to assure the synthesis of FeS₂, we did another XRD test on the electrodeposited film solely, by scrapping the adhered film, and its analysis using an X'Pert Pro X-ray powder diffractometer ($\lambda=1.54 \text{ \AA}$; Cu K α beam).

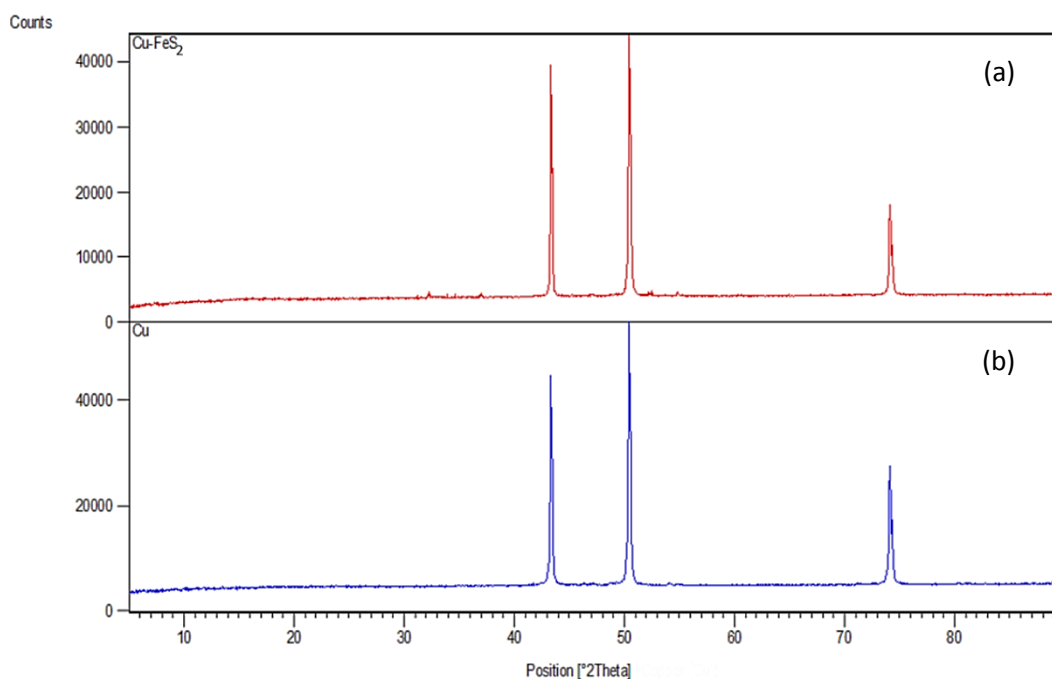


Figure S2. XRD patterns of: (a) FeS₂ thin-film electrodeposited on the copper substrate, (b) Cu without thin film [recorded for the substrate before the electrodeposition process].

To reconfirm the electrodeposition of FeS₂ and the formation of both pyrite (p) and marcasite (m) phases, we also carried out extra analyses through Raman spectroscopy [6], by employing a Rigaku FirstGuard hand-held spectrometer with a 1064 nm laser. Regarding the presence of both p and m phases in the electrodeposited film (**Fig. 2a** and **b**), it is worth mentioning that the recent studies indicate that the application of the mixed phases (p/m) in

the preparation of the photoelectrode, exhibits a better activity than that of using just p or m phase in the film [7-8].

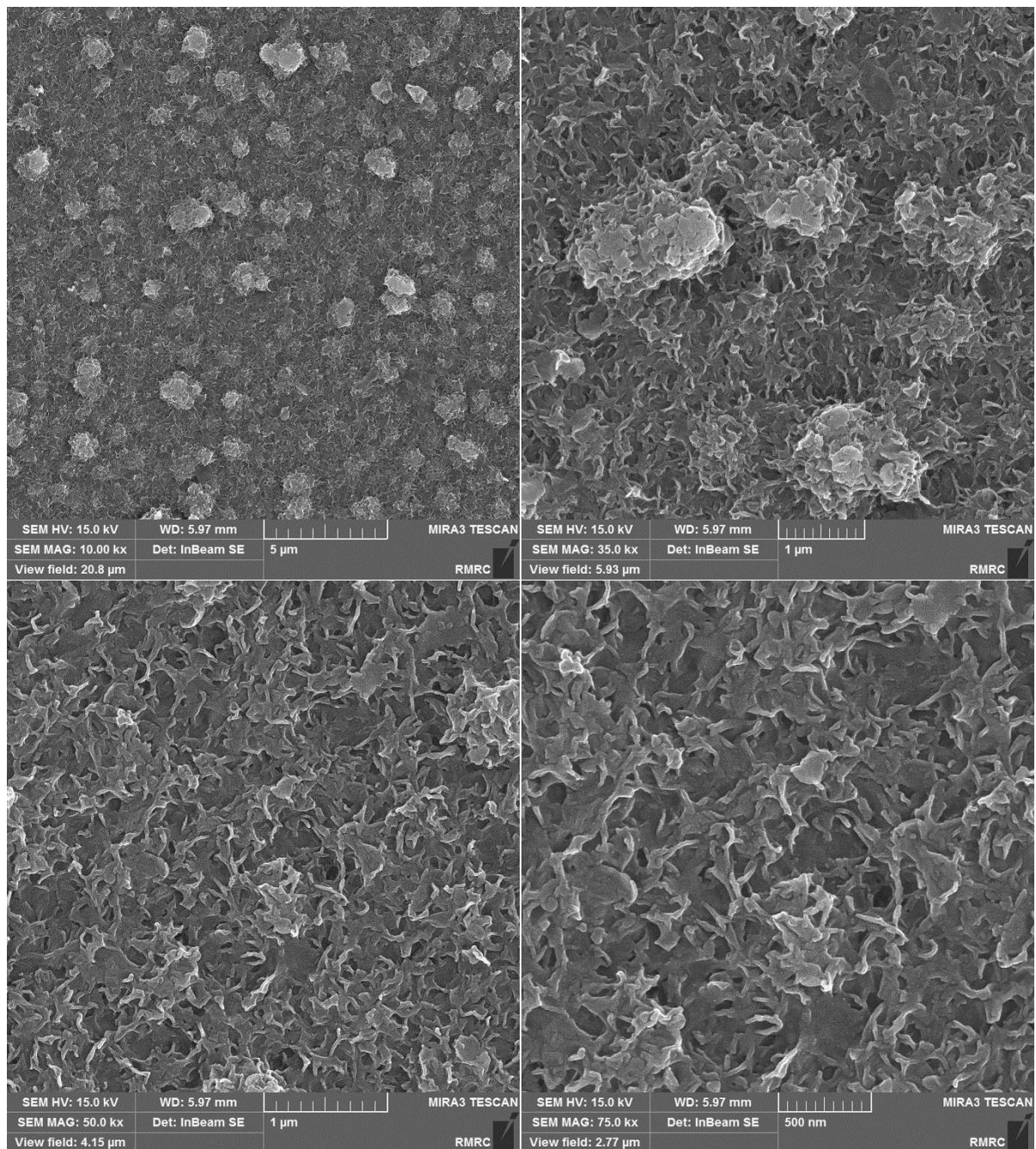


Figure S3. SEM images (Top-view) of FeS₂ thin-film electrodeposited on the copper substrate, taken at different magnifications.

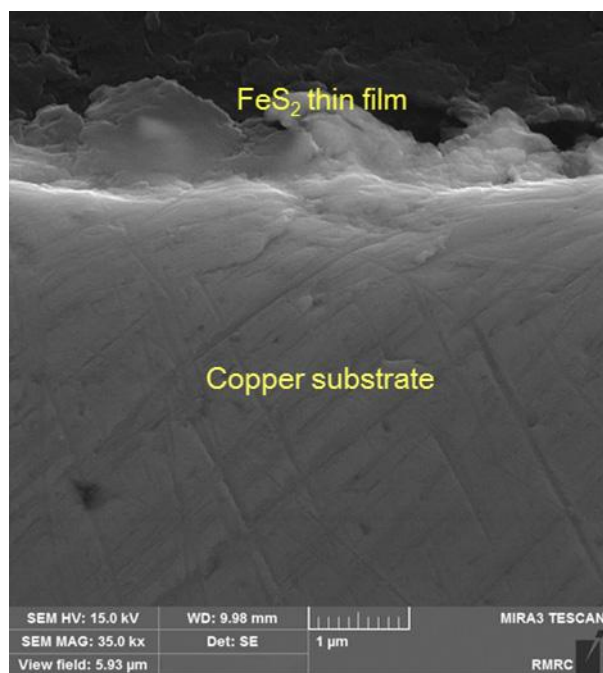


Figure S4. Cross-sectional SEM image (Bird's-eye view) of the porous FeS₂ thin-film electrodeposited on the Cu substrate.

To determine the ability of film in the absorption of photons, the film was electrodeposited on a conductive transparent substrate, viz. FTO (fluorine-doped tin oxide; SOLARONIX, electrical resistance: 10 Ω/sq) and its spectrum was recorded in the transmission mode using a Pharmacia Biotech Ultrospec 4000 UV–visible spectrometer (undeposited FTO was used as the blank/standard). The extinction coefficient of the film (α) was calculated through Lambert formula (**eq. 4**), using the absorption data (A) and film thickness ($\ell \approx 1\mu\text{m}$; **Fig. 2d**) as follows [9]:

$$A = \left(\frac{\alpha}{\ln 10}\right) \times \ell \quad (4)$$

The film bandgap was also determined through Tauc's approach [9]; see **Fig. S5**.

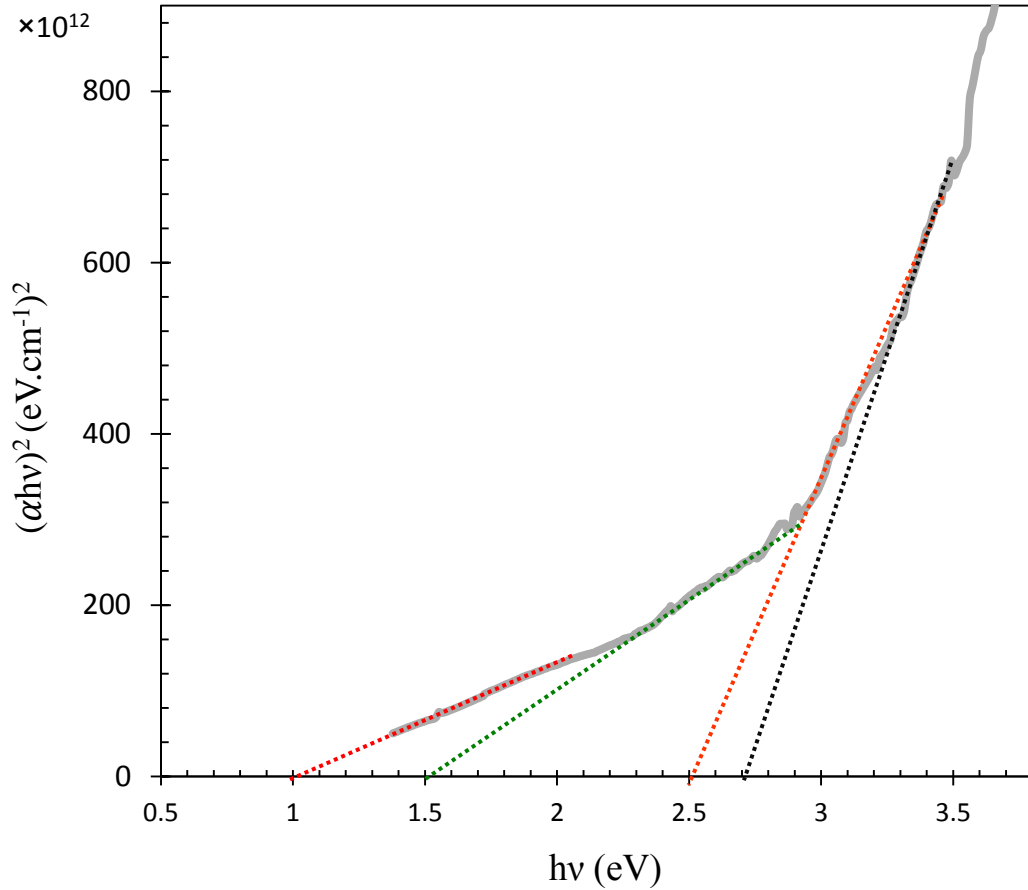


Figure S5. Tauc's plot of the electrodeposited FeS₂ thin-film.

Based on this diagram, one could estimate several bandgaps with the values ~1, 1.5, 2.5 and 2.7 eV for the electrodeposited FeS₂ thin-film. In this semiconducting material, the lowest energy gap is due to the indirect, whereas the higher values are ascribed to direct transitions [10-11]. The multi-bandgap structure recognized for FeS₂, has been also witnessed elsewhere [10-11] and seems to be the characteristic of this energy material, and a result of its intrinsic ability to form a metal or sulfur vacancy [12]: by the formation of vacancy, some surface states could be created in the forbidden region, and the electronic transitions at different energy values are consequently rationalized. Concerning the experiencing several energy-gap values, it is worth noting that the inhomogeneity in the material's phase/morphology is another reason, which should also be taken into consideration; the latter justifies why different synthesis procedure would not usually result in the same bandgap value [3].

3- Electrochemical/photoelectrochemical tests

All electrochemical/photoelectrochemical tests, including Mott-Schottky, linear sweep voltammetry (LSV) as well as chopped LSV, open circuit potential (OCP), transient photocurrent, etc. were conducted using the mentioned electrochemical instrument operating with Ivium Soft 2.662. The tests were carried out in a 3-electrode system (WE: Cu/FeS₂, RE: Ag/AgCl (3M), CE: Pt foil (2.5 cm²), electrolyte: 0.1 M Na₂SO₄ aqueous solution (pH 6.5) [14]). To avoid the complication of the photoelectrode response –which is arising from its Schottky junction [metallic/semiconducting] nature, the semiconducting portion of the photodevice (FeS₂ film) was just immersed into the solution and the metallic/uncoated parts were insulated by painting with a nitrocellulose lacquer. For photoelectrochemical tests, the intensity of incident photons was set at 100mW/cm² and a monochromatic 434 nm high power LED was used as a light source [15]. To record the chopped LSV, the light path was manually blocked/unblocked during the test (scan rate: 1mV/sec, chopping period: 25 sec on/off).

4- N₂-photofixation, ammonia analysis, and control experiments

To carry out N₂-fixation process, an ultra-pure N₂ gas (99.999%) was employed as nitrogen feed [to remove possible impurities in the N₂ gas-stream, it is also recommended to employ a couple of traps, one for ammonia (filled by dilute acid solution, 1mM H₂SO₄) and the other for NO_x (filled by distilled water); Energy Environ. Sci. 2017, 10, 2516–2520 and ACS Catalysis, 2018, 9, 336–344]. Nitrogen conversion into ammonia was conducted under xenon light irradiation (100mW/cm²) inside a homemade upright double-walled cylindrical glass reactor (capacity: 50 ml) [16], on the photodevice (FeS₂/Cu) surface–fixed at the center of the reaction medium. During the test, using a thin gas-conducting tube with several tiny holes created in its wall [see **Fig. 5**, the inset], N₂ molecules were smoothly bubbled into the reaction medium–containing 1.2mM sulfite hole scavenger [17]–directly upon the photodevice surface. Here, the authors used xenon light source [Ushio Xenon Short Arc Lamp, 500 W tunable power operating at 1/12 of its maximum power], because its spectrum is close to that of sun [18]. Moreover, by adjusting the distance between the photoreactor and light source and measuring the intensity of striking photons through a Melles Griot 13 PEM 001/J power meter, the intensity was set at 100mW/cm² (1 sun).

To measure the quantity of ammonia, we employed Nessler's spectrophotometric approach–which is a sensitive as well as standard (JB7478-87) method for the analysis of ammonia in alcohol-free environments [15, 19-20]. Here, the ammonia concentration was determined spectrophotometrically at 425 nm, after its conversion to “ammonobasic mercuric iodide”, using a Pharmacia Biotech Ultrospec 3100 UV–Vis. spectrometer. Besides the Nessler's method (**Fig. S6**), the amount of ammonia product was determined through H-NMR studies (**Fig. S7**) and a good correlation was observed between both methods (R²=0.9974).

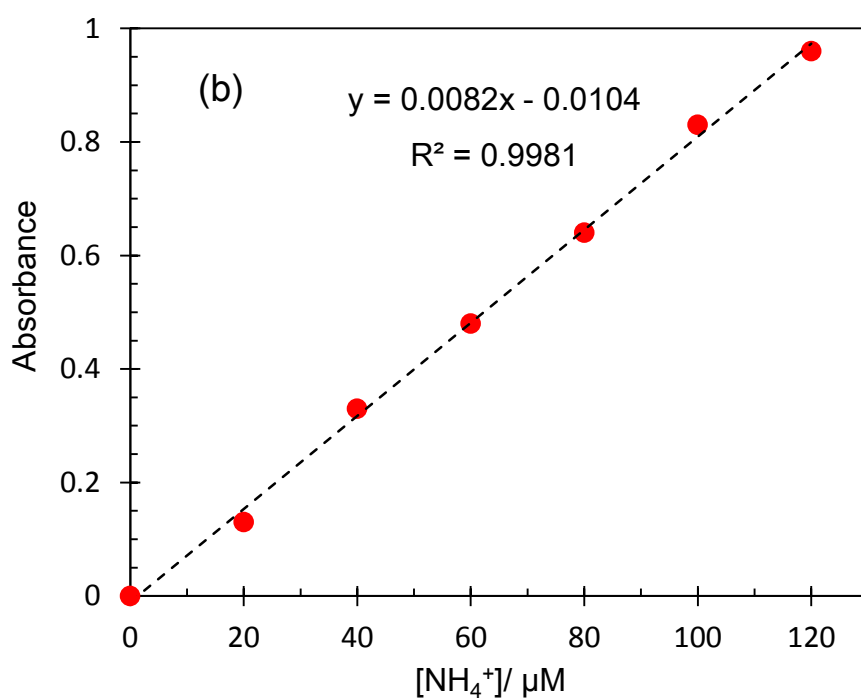
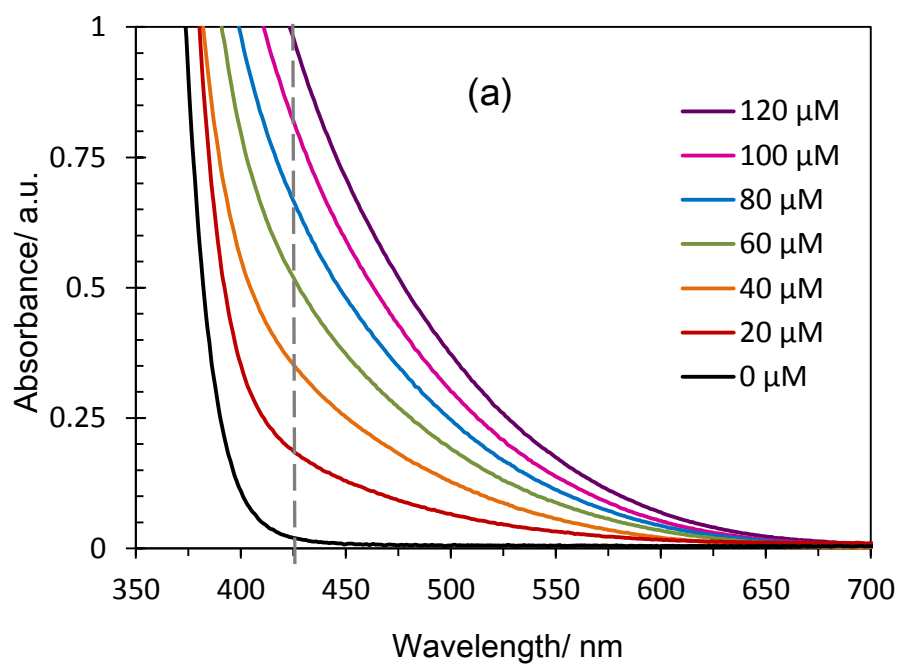


Figure S6. UV-vis (a) and calibration (b) diagrams recorded in this study for determination of ammonia concentration through Nessler's approach (in the calibration diagram, absorbance was read at 425 nm).

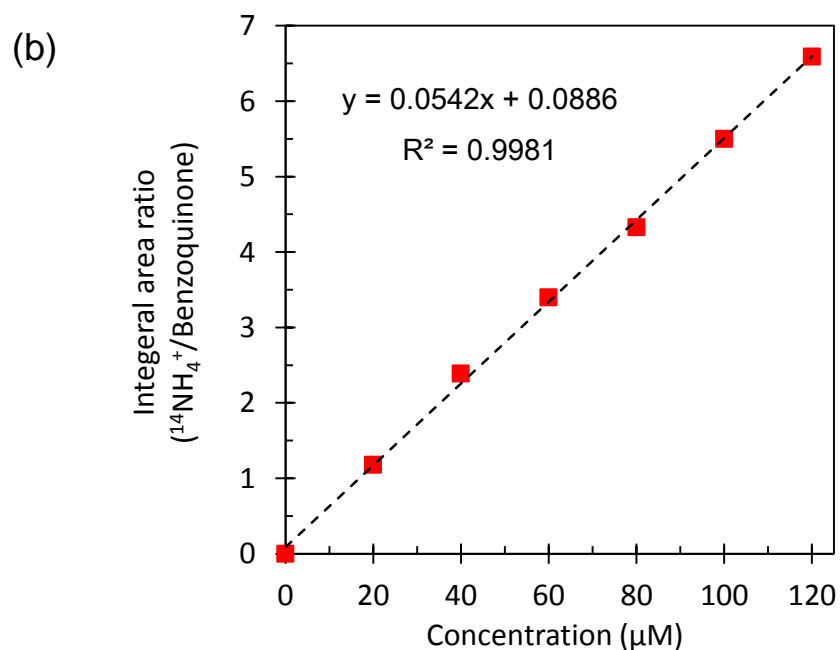
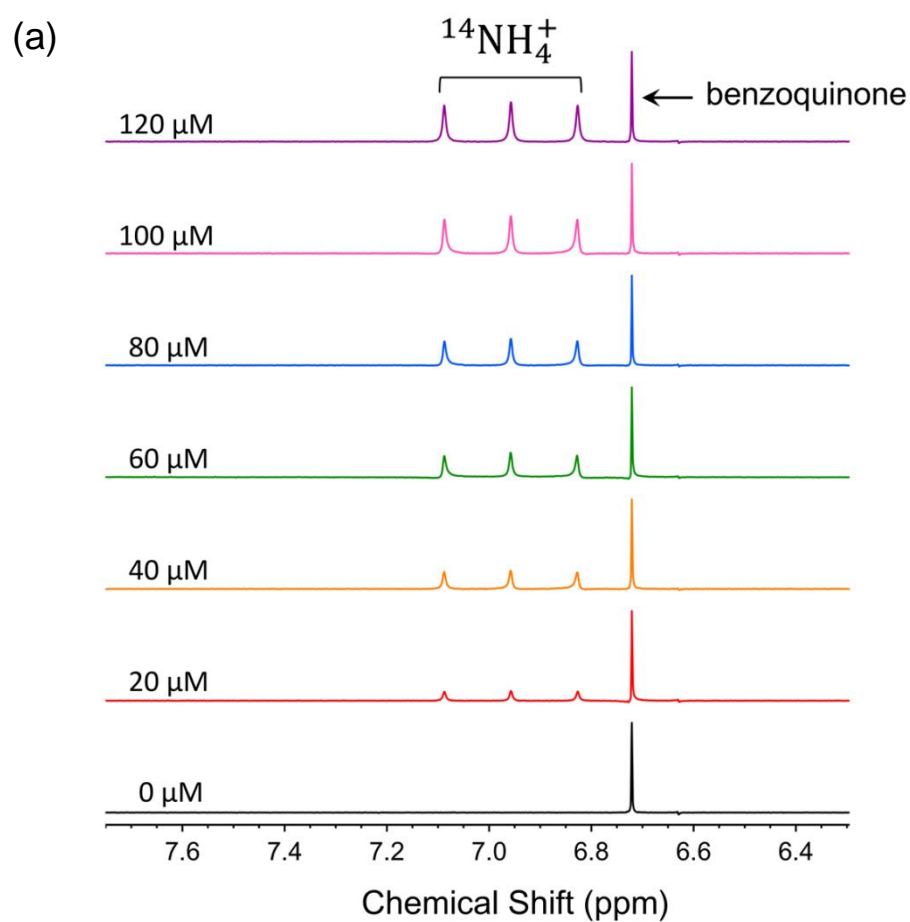


Figure S7. ^1H NMR spectra of ammonium ($^{14}\text{NH}_4^+$) aqueous media measured at different known concentrations (a) in the presence of p-benzoquinone [$3.85 \mu\text{M}$, serving as a reference for integral area determination]. (b) Calibration diagram for the ammonium solutions, depicted using ^1H NMR data.

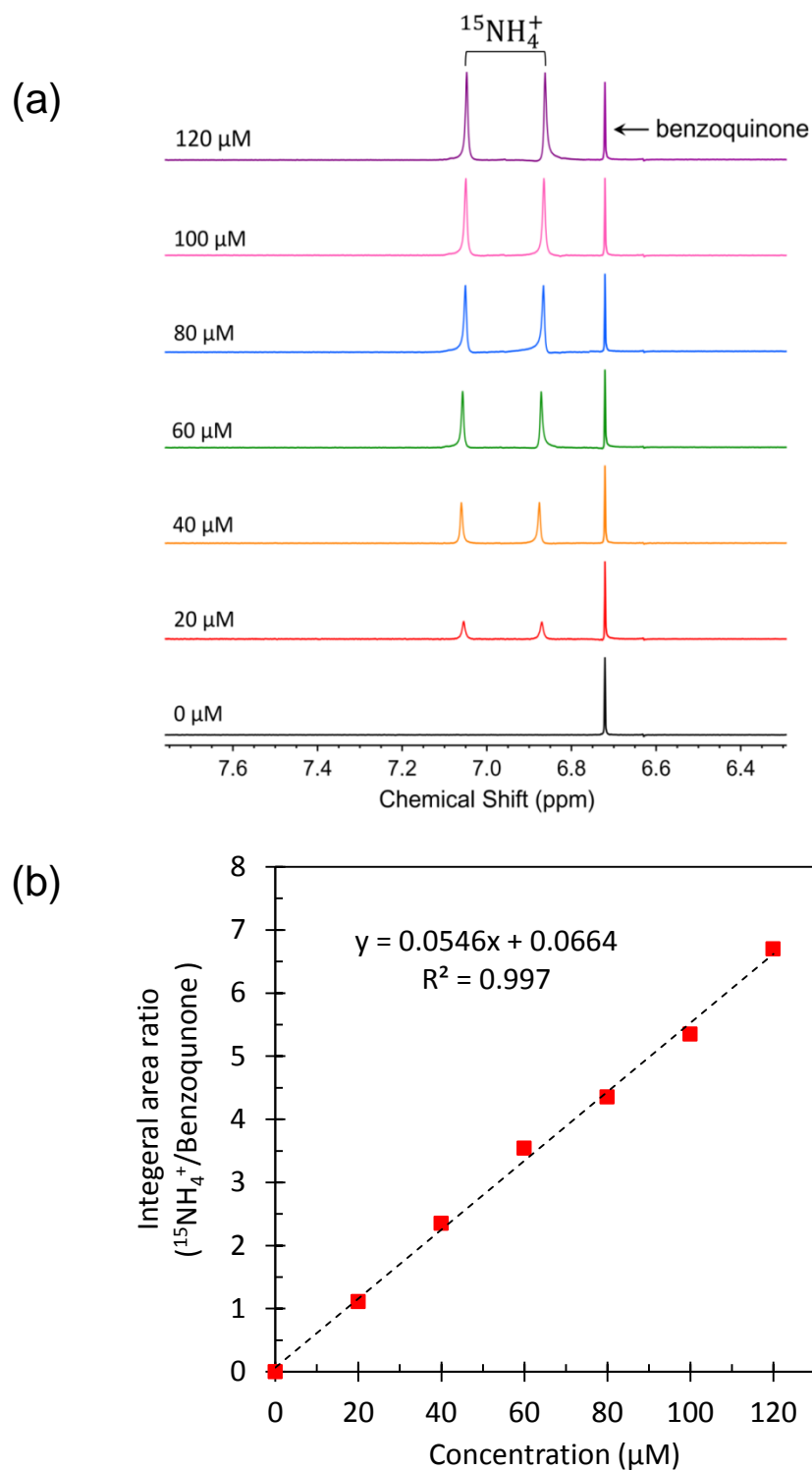


Figure S8. ^1H NMR spectra of ammonium- ^{15}N sulfate (Sigma-Aldrich; $(^{15}\text{NH}_4)_2\text{SO}_4$; 98 atom%) aqueous solutions measured at different known ammonium concentrations (a) in the presence of p-benzoquinone (3.85 μM). (b) Calibration diagram plotted for $^{15}\text{NH}_4^+$ solutions using ^1H NMR data.

It is worth mentioning that under the same reaction periods, approximately equal quantity of ammonium was produced for both $^{14}\text{N}_2$ and $^{15}\text{N}_2$ feed; e.g. for 3-h operation of the photoreactor, 6.34 and 6.52 μM ammonium were synthesized using $^{14}\text{N}_2$ and $^{15}\text{N}_2$ feed, respectively. This evidence approves that the origin of ammonium product is indeed nitrogen gas not impurity [Angew. Chem. Int. Ed. 2019, 131, 2638–2642; Energy Environ. Sci. 2017, 10, 2516–2520; Nat. Catal. 2019, 2, 448; Nano Energy, 2019, 63, 103886].

Furthermore, it should be remarked that in the absence of N_2 feed, hole-scavenger additive, photodevice or light source, no ammonia was produced; **Fig. S9**. Under normal conditions [system illumination, blowing N_2 gas and the presence of photodevice and hole-scavenger additive], however, the reactor generated ammonia, and the concentration of product was continuously increased with time.

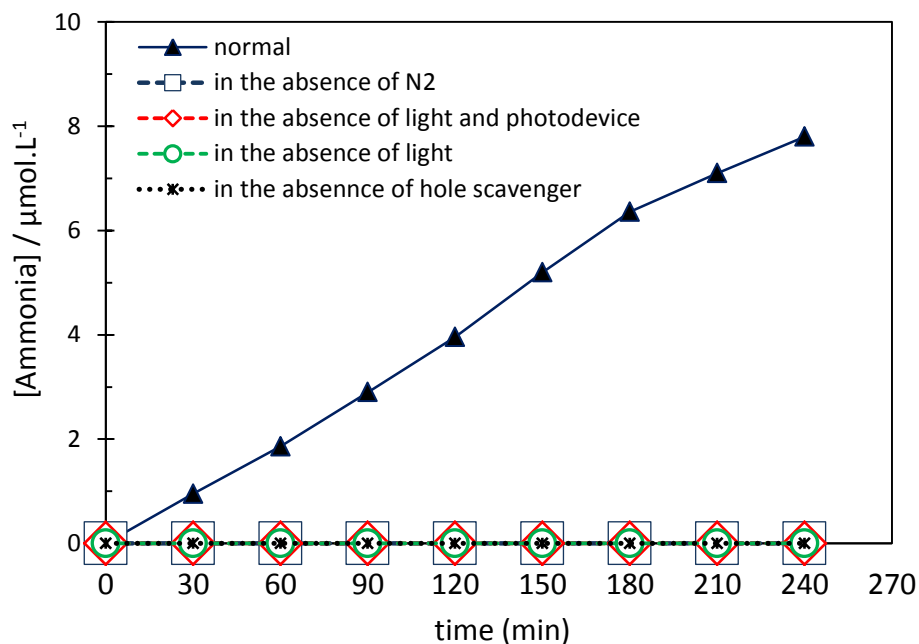


Figure S9. Control experiments carried out for the synthesis of ammonia upon FeS_2/Cu monolithic photodevice.

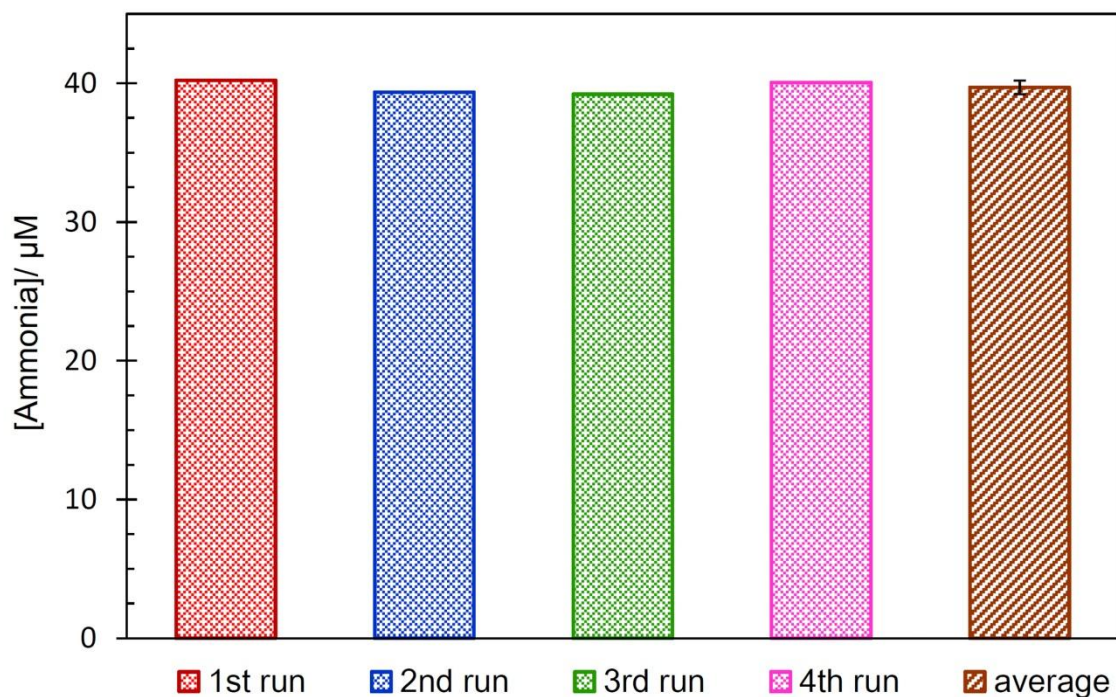


Figure S10: Stability/durability test of the photodevice for prolonged application to produce ammonia, recorded for four 24-h successive operations of the reactor.

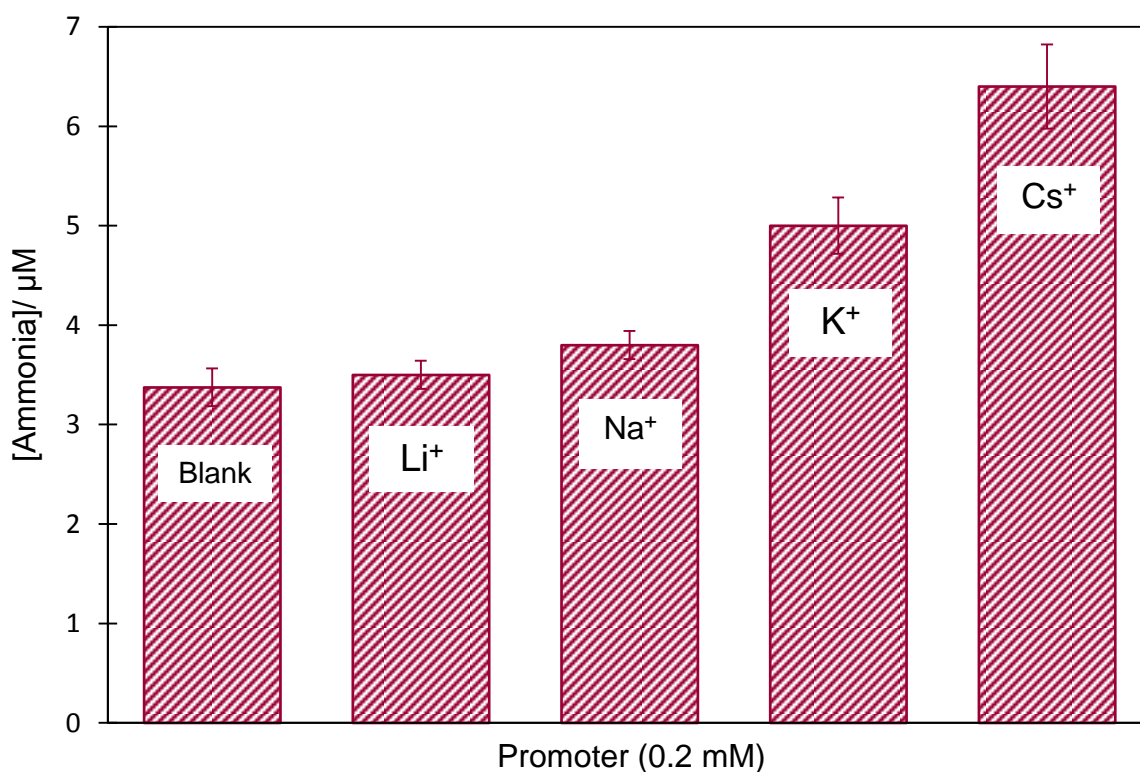


Figure S11: Promotion effect of alkali metal cations on the photodevice activity to produce ammonia [0.2 mM was taken because it was the optimum concentration for the system under study; see Fig. 7 of the main article].

5- Electrostatic promotion of the ammonia photosynthesis: applying a non-faradic potential bias to the photodevice

To apply a non-faradic/electrostatic potential bias to the photodevice, we used the following setup (**Fig. S12**) and utilized a PROVA 8000 instrument –a programmable dc power supply with maximum output 40 V. Similar to other photoelectrochemical tests [p. S8, **Section 3**], the OCP measurements were conducted in a 0.1 M Na_2SO_4 solution. In the case of higher potential values, the N_2 -photofixation tests were carried out by employing a high-voltage power source, viz. EPS 600 (Pharmacia Biotech).

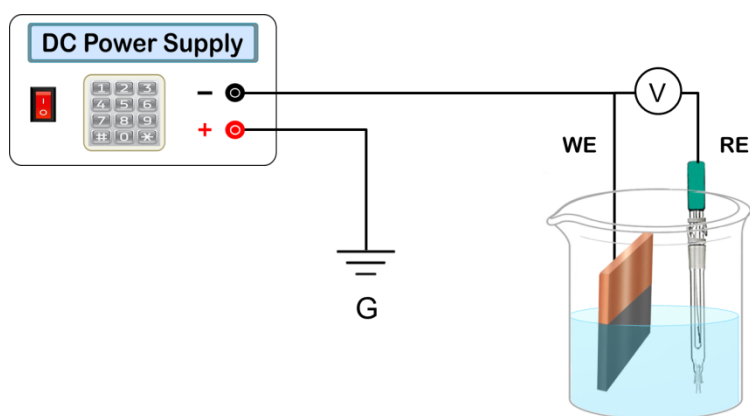


Figure S12: Schematic representation of applying a non-faradic/electrostatic dc potential bias to the photodevice (for accurate measurement of OCP data, the Potentio-Galvanostat instrument is employed).

Due to the absence of counter electrode (see **Fig. S12**), no electrical charges cross the photoelectrode/electrolyte interface and the excess charges [being electrostatically supplied by the power source] are just accumulated in the photodevice. The non-faradic nature of the bias potentials illustrated in **Fig. 12** was also confirmed by other control experiments [see **Fig. S14**].

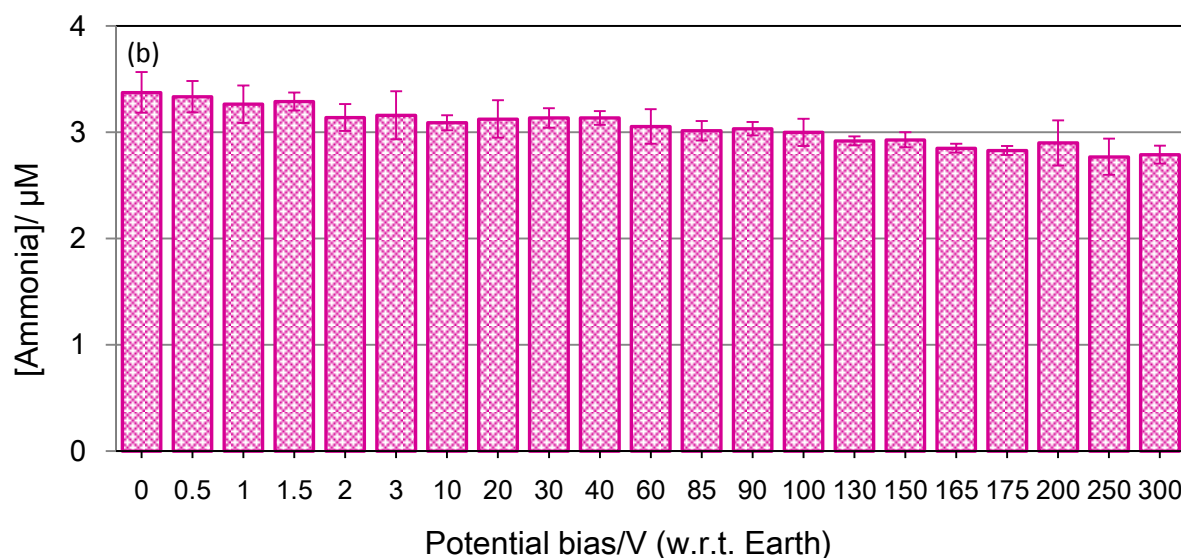
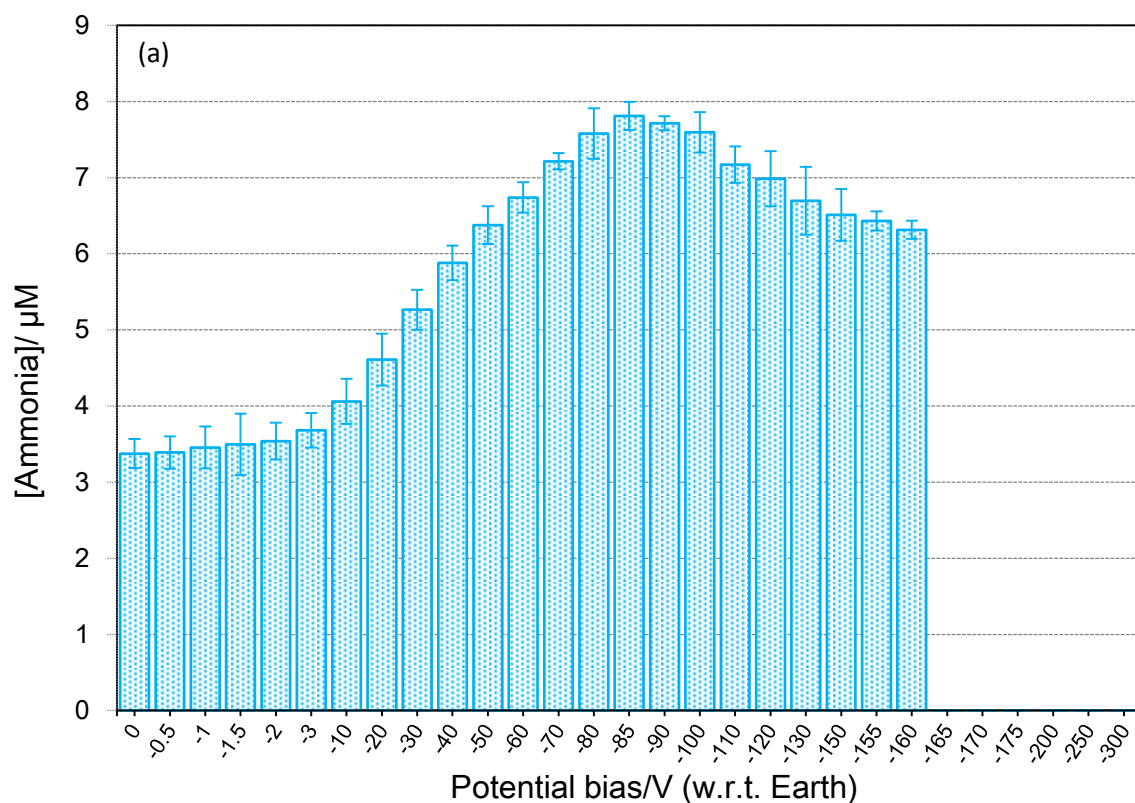


Figure S13: Ammonia photosynthesis under negative (a) and positive (b) non-faradic potential biases, recorded in a wide potential range, 0 to $-300 V_{\text{Earth}}$.

This figure indicates that at potentials more negative than $-160 V$, the synthesis of ammonia is abruptly stopped. In the case of positive biases, however, by applying more positive values, the activity of photodevice is slightly diminished.

Regarding the non-faradic nature of the electrical bias applied in the present work, it should be emphasized that in the absence of photon, no ammonia was produced under either negative or positive biased conditions; see **Fig. S14**. This empirical evidence clearly indicates that the bias potential applied in the present work is indeed non-faradic [electrostatic].

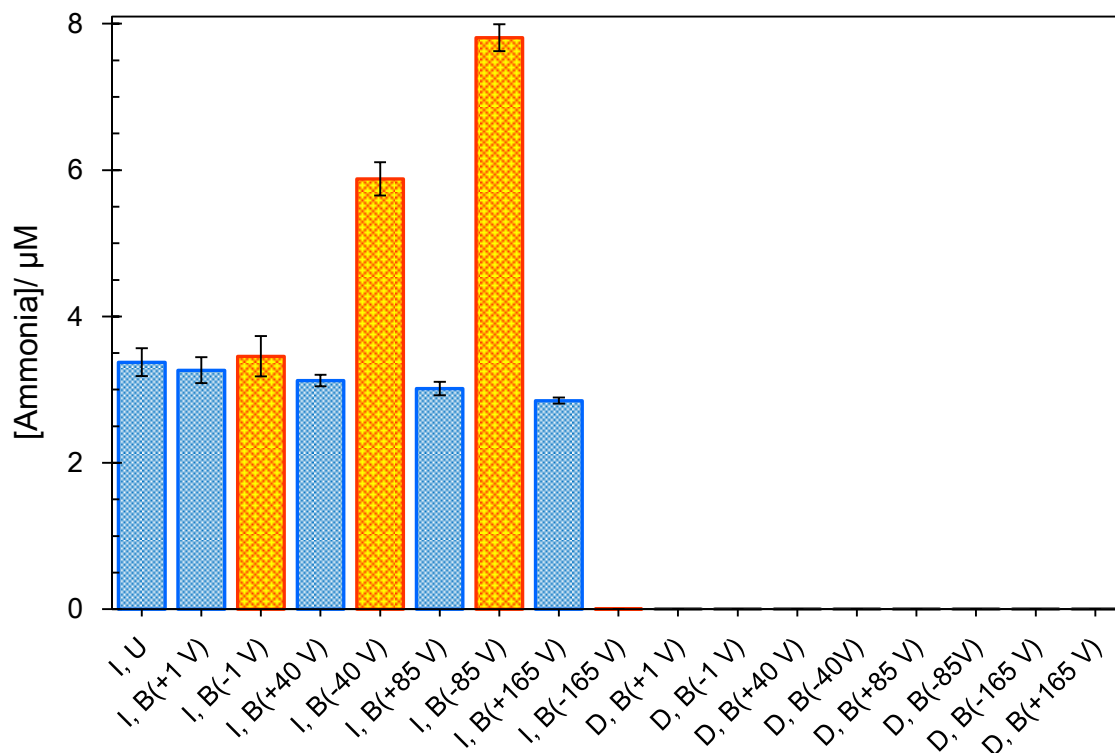


Figure S14: Extra control experiments carried out for the ammonia synthesis under biased (B) and un-biased (U) conditions in the presence (I) and absence (D) of light [data were collected after 2 h operation of the photoreactor].

To prove the generation of sulfate as the reaction byproduct (p. S8; **eq. 5**), we also performed ion chromatographic (IC) studies, and the presence of both sulfite and sulfate anions were confirmed as two distinct peaks in the resulting chromatograms (**Fig. S15**). Here, the peak being appeared at longer retention time is ascribed to sulfate anion.

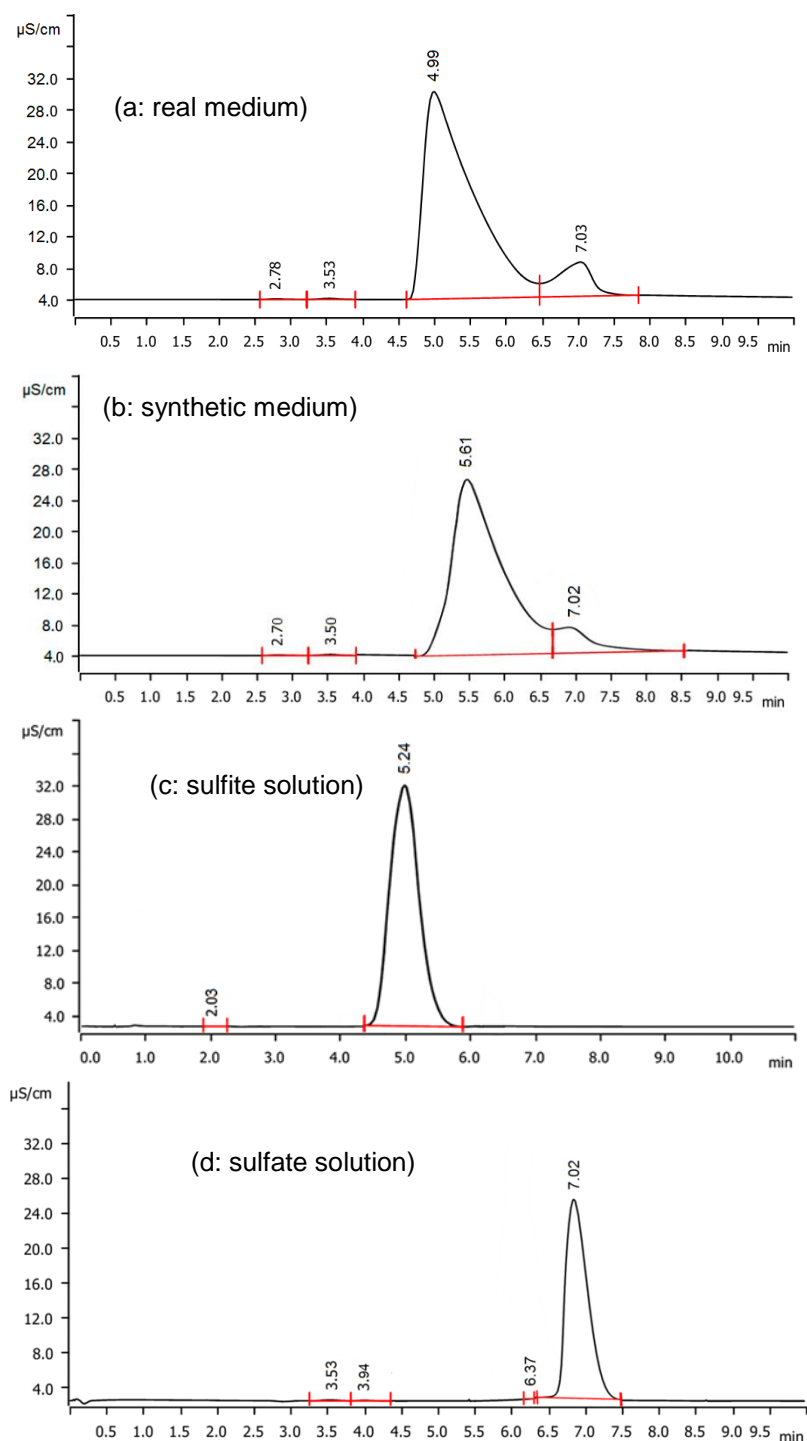


Figure S15: Ionic chromatograms recorded for various sulfite/sulfate-containing media: (a) the reaction medium after 24 h operation of the photoreactor, (b) a synthetic/simulated reaction medium (sulfite (1160 μM) + sulfate (40 μM)), (c) sulfite solution (1.2 mM), and (d) sulfate solution (1.2 mM).

The tests were conducted using a Metrohm 881 Compact IC Pro instrument; column: Metrosep A Supp 4-250/4.0, eluent: 1 mM Na_2CO_3 + 2.6 mM NaOH , flow rate: 1ml/min. To prohibit the sulfite anion oxidation and its conversion into sulfate, formaldehyde stabilizer (in a 1:1 molar ratio with respect to sulfite anion) was added to the sulfite-containing samples [22].

Table S1. A comparison of the ability of photoelectrochemical devices/reactors to synthesis ammonia between this work [utilizing low-price/earth-abundant/eco-friendly energy materials] and other related works reported in the literature.

Photocatalyst	\bar{R}_{NH_3} (nmol/h.cm ⁻²)	Bias voltage	Hole scavenger additive	Light source	Ref.
Cu/FeS ₂	79.3 ^a	–	SO ₃ ²⁻	500 W Xenon Lamp (100 mWcm ⁻²)	This work
Cu/FeS ₂	195.2	non-Faradic (85 V vs. Earth)	SO ₃ ²⁻	500 W Xenon Lamp (100 mWcm ⁻²)	This work
Au-NPs/bSi/Cr	79	–	SO ₃ ²⁻	300 W Xenon Lamp (200 mWcm ⁻²)	17
Au-NPs/Nb-SrTiO ₃ /Ru	1.1	–	Ethanol	Xenon Lamp	23
Au-NPs/Nb-SrTiO ₃ /Zr/ZrO _x	6.5	–	–	Xenon Lamp	24
diamond	17	–	–	450 W high-pressure Hg/Xe lamp	25
TiO ₂ /Au/a-TiO ₂	13.4	–	–	300 W Xenon Lamp (100 mWcm ⁻²)	26
R-BiOI	140	Faradic (0.4 V vs. RHE)	–	Light source: not reported (100 mWcm ⁻²)	27
Au-PTFE/TS	1111.7	Faradic (-0.2 V vs. RHE)	SO ₃ ²⁻	Xenon Lamp (100 mWcm ⁻²)	28
Au-Ag ₂ O	165.88	–	–	(100 mWcm ⁻²)	29
MoS ₂ @TiO ₂	1470	Faradic bias (-0.3 V w.r.t RHE)	–	(100 mWcm ⁻²)	30
Au-NPs/SrTiO ₃ -photoanode & Zr Coil cathode	10	Faradic bias (1.0 V w.r.t RHE)	–	Xenon lamp (410 – 800 nm)	31

^a Measured after 2-hr operation of the photoreactor in the absence of Cs⁺ promoter. In the presence of promoter (0.2 mM), the rate of ammonia production becomes approximately doubled ($\bar{R}_{\text{NH}_3} = 163.2$ nmol/h.cm⁻²).

Concerning the data presented in **Table S1**, the following points are remarkable:

- 1- To attain an effective synthesis of ammonia through the photoelectrochemical approach, *the manner of bubbling of N₂ gas into the reaction medium [system design] is crucial*: during the nitrogen fixation process, since N₂ molecules are heterogeneously reduced at the device/solution interface, more ammonia could be synthesized if the blowing of N₂ molecules become directly conducted onto the electrode surface [**Fig. 5**, the inset]. Otherwise, the system performance could dramatically diminish if the bubbling is carried out improperly [under this situation, since a slight portion of nitrogen molecules can reach the electrode surface, most of them remain unreacted and escape from the reaction medium].
- 2- By applying a bias voltage to the photodevice, more ammonia can be synthesized. This electrical bias can be employed in two ways: faradic and non-faradic (electrostatic). In comparison to the latter case [non-faradic/electrostatic], during the faradic processes, electricity is indeed used up to produce extra ammonia.

- 3- Under non-faradic (electrostatic) bias, without consuming electricity at the device interface [see **Fig. S12** and note its discussion], just by altering OCP (raising Fermi level; see the main text), a significant promotion is achieved in the synthesis of ammonia.
- 4- In an alternative route, the activity of photodevice can be chemically [non-electrically] enhanced by adding promoter species into the reaction medium.

References:

- [1] M. Lashgari, M. R. Arshadi, M. Biglar, Comparative studies of some heterocyclic compounds as corrosion inhibitors of copper in phosphoric acid media, *Chem. Eng. Commun.* 2010, **197**, 1303–1314.
- [2] P. Kar, S. Farsinezhad, X. Zhang, K. Shankar, Anodic Cu₂S and CuS nanorod and nanowall arrays: preparation, properties and application in CO₂ photoreduction, *Nanoscale*, 2014, **6**, 14305–14318.
- [3] Jana, P. Mondal, S. Tripathi, A. Mondal, Electrochemical synthesis of FeS₂ thin film: An effective material for peroxide sensing and terephthalic acid degradation, *J. Alloys Compd.*, 2015, **646**, 893–899.
- [4] B. Chakraborty, B. Show, S. Jana, B. C. Mitra, S. K. Maji, B. Adhikary, N. Mukherjee, A. Mondal, Cathodic and anodic deposition of FeS₂ thin films and their application in electrochemical reduction and amperometric sensing of H₂O₂, *Electrochim. Acta*, 2013, **94**, 7–15.
- [5] D. R. Lide, "Electrochemical Series", in *CRC Handbook of Chemistry and Physics*, 89th Edition (Internet Version 2009) CRC Press; Taylor & Francis Group.
- [6] X. Liu, J. Y. L. Ho, M. Wong, H. S. Kwok, Z. Liu, Synthesis, characterization and fabrication of ultrathin iron pyrite (FeS₂) thin films and field-effect transistors, *RSC Adv.*, 2016, **6**, 8290–8296.
- [7] L. Wu, N. Y. Dzade, L. Gao, D. O. Scanlon, Z. Öztürk, N. Hollingsworth, B. M. Weckhuysen, E. J. M. Hensen, N. H. De Leeuw, J. P. Hofmann, Enhanced photoresponse of FeS₂ films: the role of marcasite–pyrite phase junctions, *Adv. Mater.* 2016, **43**, 9602–9607.
- [8] D. G. Moon, S. Rehan, S. Y. Lim, D. Nam, I. Seo, J. Gwak, H. Cheong, Y. S. Cho, Y. Lee, S. J. Ahn, Structural, optical and electrical impacts of marcasite in pyrite thin films, *Sol. Energy*, 2018, **159**, 930–939.
- [9] M. Lashgari, N. Shafizadeh, P. Zeinalkhani, A nanocomposite p-type semiconductor film for possible application in solar cells: photo-electrochemical studies, *Sol. Energy Mater. Sol. Cells*, 2015, **137**, 274–279.
- [10] H. A. Macpherson, C. R. Stoldt, Iron pyrite nanocubes: size and shape considerations for photovoltaic application, *ACS Nano*, 2012, **6**, 8940–8949.
- [11] G. Zhai, R. Xie, H. Wang, J. Zhang, Y. Yang, H. Wang, X. Li, X. Liu, B. Xu, Effect of capping ligands on the optical properties and electronic energies of iron pyrite FeS₂ nanocrystals and solid thin films, *J. Alloys Compd.*, 2016, **674**, 9–15.
- [12]] A. Krishnamoorthy, F. W. Herbert, S. Yip, K. J. Van Vliet, B. Yildiz, Electronic states of intrinsic surface and bulk vacancies in FeS₂, *J. Phys.: Condens. Matter*, 2013, **25**, 045004; DOI: 10.1088/0953-8984/25/4/045004

- [13] L. Ji, M. D. McDaniel, S. Wang, A. B. Posadas, X. Li, H. Huang, J. C. Lee, A. A. Demkov, A. J. Bard, J. G. Ekerdt, E. T. Yu, A silicon-based photocathode for water reduction with an epitaxial SrTiO₃ protection layer and a nanostructured catalyst, *Nat. Nanotechnol.*, 2015, **10**, 84; DOI: 10.1038/NNANO.2014.277
- [14] G. Ghadimkhani, N. R. de Tacconi, W. Chanmanee, C. Janaky, K. Rajeshwar, Efficient solar photoelectrosynthesis of methanol from carbon dioxide using hybrid CuO–Cu₂O semiconductor nanorod arrays, *Chem. Commun.*, 2013, **49**, 1297–1299.
- [15] M. Lashgari, P. Zeinalkhani, Ammonia photosynthesis under ambient conditions using an efficient nanostructured FeS₂/CNT solar-energy-material with water feedstock and nitrogen gas, *Nano Energy*, 2018, **48**, 361–368.
- [16] M. Lashgari, P. Zeinalkhani, Photocatalytic N₂ conversion to ammonia using efficient nanostructured solar-energy-materials in aqueous media: A novel hydrogenation strategy and basic understanding of the phenomenon. *Appl. Catal. A*, 2017, **529**, 91–97.
- [17] M. Ali, F. Zhou, K. Chen, C. Kotzur, C. Xiao, L. Bourgeois, X. Zhang, D. R. MacFarlane, Nanostructured photoelectrochemical solar cell for nitrogen reduction using plasmon-enhanced black silicon, *Nat. Commun.*, 2016, **7**, 11335, DOI: 10.1038/ncomms11335
- [18] M. Lashgari, M. Ghanimati, Efficient mesoporous/nanostructured Ag-doped alloy semiconductor for solar hydrogen generation, *J. Photonics Energy*, 2014, **4**, 044099-1; DOI: 10.1117/1.JPE.4.044099; M. K. Nazeeruddin, A. Kay, I. Rodicio, R. Humpbry-Baker, E. Müller, P. Liska, N. Vlachopoulos, M. Grätzel, Conversion of light to electricity by cis-XzBis(2,2'-bipyridyl-4,4'-dicarboxylate)ruthenium(II) charge-transfer sensitizers (X = Cl⁻, Br⁻, I⁻, CN⁻, and SCN⁻) on nanocrystalline TiO₂ electrodes, *J. Am. Chem. Soc.*, 1993, **115**, 6382–6390.
- [19] X. Gao, Y. Wen, D. Qu, L. An, S. Luan, W. Jiang, X. Zong, X. Liu, Z. Sun, Interference effect of alcohol on Nessler's reagent in photocatalytic nitrogen fixation, *ACS Sustainable Chem. Eng.*, 2018, **6**, 5342–5348.
- [20] N. Zhang, A. Jalil, D. Wu, S. Chen, Y. Liu, C. Gao, W. Ye, Z. Qi, H. Ju, C. Wang, X. Wu, L. Song, J. Zhu, Y. Xiong, Refining defect states in W₁₈O₄₉ by Mo doping: a strategy for tuning N₂ activation towards solar-driven nitrogen fixation, *J. Am. Chem. Soc.* 2018, **140**, 9434–9443.
- [21] A.C. Nielander et al, A versatile method for ammonia detection in a range of relevant electrolytes via direct nuclear magnetic resonance techniques, *ACS Catal.*, 2019, **9**, 5797–5802.
- [22] M. Lindgren, A. Cedergren, J. Lindberg, Conditions for sulfite stabilization and determination by ion chromatography, *Anal. Chim. Acta*, 1982, **141**, 279–286.
- [23] T. Oshikiri, K. Ueno, H. Misawa, Plasmon-induced ammonia synthesis through nitrogen photofixation with visible light irradiation, *Angew. Chem. Int. Ed.*, 2014, **53**, 9802–9805.
- [24] T. Oshikiri, K. Ueno, H. Misawa, Selective dinitrogen conversion to ammonia using water and visible light through plasmon-induced charge separation, *Angew. Chem. Int. Ed.*, 2016, **55**, 3942–3946.
- [25] D. Zhu, L. Zhang, R. E. Ruther, R. J. Hamers, Photo-illuminated diamond as a solid-state source of solvated electrons in water for nitrogen reduction, *Nat. Mater.*, 2013, **12**, 836–841.
- [26] C. Li, T. Wang, Z-J. Zhao, W. Yang, J. Li, A. Li, Z. Yang, G. A. Ozin, J. Gong, Promoted fixation of molecular nitrogen with surface oxygen vacancies on plasmon-enhanced TiO₂ photoelectrodes, *Angew. Chem. Int. Ed.*, 2018, **57**, 5278–5282.

- [27] Y. Bai, H. Bai, K. Qu, F. Wang, P. Guan, D. Xu, W. Fan, W. Shi, In-situ approach to fabricate BiOI photocathode with oxygen vacancies: understanding the N₂ reduced behavior in photoelectrochemical system, *Chem. Eng. J.*, 2019, **362**, 349–356.
- [28] J. Zheng, Y. Lyu, M. Qiao, R. Wang, Y. Zhou, H. Li, C. Chen, Y. Li, H. Zhou, S.P. Jiang, S. Wang, Photoelectrochemical synthesis of ammonia on the aerophilic-hydrophilic heterostructure with 37.8% efficiency, *Chem.*, 2019, **5**, 617–633.
- [29] M. Nazemi, M. A. El-Sayed, Plasmon-enhanced photo(electro)chemical nitrogen fixation under ambient conditions using visible light responsive hybrid hollow Au-Ag₂O nanocages, *Nano Energy*, 2019, **63**, 103886.
- [30] W. Ye, M. Arif, X. Fang, M. A. Mushtaq, X. Chen, D. Yan, An efficient photoelectrochemical route for the ambient reduction of N₂ to NH₃ based on nanojunctions assembled from MoS₂ nanosheets and TiO₂, *ACS Appl. Mater. Interfaces*, 2019, **11**, 28809–28817.
- [31] T. Oshikiri, K. Ueno, H. Misawa, Ammonia photosynthesis via an association pathway using a plasmonic photoanode and a zirconium cathode, *Green Chem.* 2019, **21**, 4443–4448.